Obrabotka metallov (tekhnologiya, oborudovanie, instrumenty) = Metal Working and Material Science. 2026 vol. 28 no. 2 pp. 298–317
ISSN: 1994-6309 (print) / 2541-819X (online)
DOI: 10.17212/1994-6309-2026-28.2-298-317

NSTU NETI

Obrabotka metallov - Metal Working and Material Science

Journal homepage: http://journals.nstu.ru/obrabotka_metallov

Regularities of structure formation and evolution of mechanical properties of copper alloys under single-pass friction stir processing with controlled heat removal

Andrey Cheremnov [a, *], *Andrey Chumaevskii* [b], *Evgeny Knyazhev* [c], *Sergei Tarasov* [d], *Evgeny Kolubaev* [e]

Institute of Strength Physics and Materials Science of Siberian Branch of Russian Academy of Sciences, Akademichesky ave, 2/4, Tomsk, 634055, Russian Federation

[a] https://orcid.org/0000-0003-2225-8232, amc@ispms.ru; [b] https://orcid.org/0000-0002-1983-4385, tch7av@gmail.com;
[c] https://orcid.org/0000-0002-1984-9720, clothoid@ispms.tsc.ru; [d] https://orcid.org/0000-0003-0702-7639, tsy@ispms.ru;
[e] https://orcid.org/0000-0001-7288-3656, eak@ispms.ru

ARTICLE INFO

Article history:
Received: 26 February 2026
Revised: 21 March 2026
Accepted: 23 March 2026
Available online: 15 June 2026

Keywords:
Friction stir processing
Copper alloys
Bronze
Brass
Dynamic recrystallization
Active cooling
Grain boundary strengthening.

Funding
The results were obtained under the state assignment for ISPMS SB RAS, Project No. FWRW-2026-0001.

ABSTRACT

Introduction. Friction stir processing (*FSP*) is recognized as a promising method for surface layer modification of structural copper-based alloys; however, the high thermal conductivity of this class of materials significantly complicates thermal cycle management and, consequently, microstructural control. The present work is devoted to a systematic study of the effect of controlled heat removal – both air cooling and water cooling – during single-pass *FSP* on the structural-phase state and the resulting mechanical properties of a series of commercial copper alloys. ***The purpose of the study*** is to establish the relationship between the intensity of forced cooling, the thermophysical properties of the alloys, and the resulting grain morphology in the stir zone, which determines the level of service properties of the processed materials. **Methods.** The following alloys were selected as research objects: *89 Cu–9 Al–2 Mn*, *93.35 Cu–6.5 Sn–0.15 P*, *96 Cu–3 Si–1 Mn*, and *63 Cu-37 Zn*. *FSP* was performed in a single pass on a specialized experimental setup at *ISPMS SB RAS* using a tool fabricated of the nickel-based superalloy *ZhS6U*. Active heat removal was realized by immersing the workpiece in flowing water, circulating coolant through the tool body, and directing a water jet into the contact zone; compressed air blowing was used as an alternative cooling scheme. Macro- and microstructure were investigated using optical metallography, scanning and transmission electron microscopy, X-ray diffraction analysis, and energy-dispersive spectroscopy. Mechanical properties were determined by *Vickers* microhardness measurements and uniaxial quasi-static tensile testing. **Results and Discussion.** It was established that, in all studied alloys, *FSP* leads to the formation of a recrystallized fine-grained structure with predominantly equiaxed grain morphology. The best process stability and the most pronounced strengthening were achieved for aluminum bronze *89 Cu–9 Al–2 Mn* and brass *63 Cu-37 Zn*: microhardness, and ultimate tensile strength for *89 Cu–9 Al–2 Mn* increased by 7, and 12%, respectively, and for *63 Cu-37 Zn* increased by 22, and 4%, respectively, compared to the initial condition of the alloys. It was revealed that the higher thermal conductivity of the alloys necessitates an increase in axial tool force, which expands the shoulder-affected zone and forms a wide stir zone. A pronounced grain size heterogeneity along the stir zone thickness was observed: in alloys with lower thermal conductivity under water cooling, the grain size near the root of the processed zone exceeded that near the top surface by a factor of up to 16, which is explained by differences in the rate of recrystallization arrest. Higher thermal conductivity promotes the formation of a more homogeneous grain structure, especially in the absence of forced water cooling.

For citation: Cheremnov A.M., Chumaevskii A.V., Knyazhev E.O., Tarasov S.Yu., Kolubaev E.A. Regularities of structure formation and evolution of mechanical properties of copper alloys under single-pass friction stir processing with controlled heat removal. *Obrabotka metallov (tekhnologiya, oborudovanie, instrumenty) = Metal Working and Material Science*, 2026, vol. 28, no. 2, pp. 298–317. DOI: 10.17212/1994-6309-2026-28.2-298-317. (In Russian).

*** Corresponding author**
Cheremnov Andrey M., Junior Researcher
Institute of Strength Physics and Materials Science
of Siberian Branch of Russian Academy of Sciences,
2/4 Akademichesky ave.,
634055, Tomsk, Russian Federation
Tel.: +7 913 333-72-07, e-mail: amc@ispms.ru

Introduction

Among structural metallic materials, copper-based alloys hold a unique position because of their exceptional tribological qualities under hydrodynamic lubrication conditions, good ductility, thermal conductivity, and high corrosion resistance in harsh environments [1–3]. From contact suspensions in electric cars to moving mating elements in machinery and devices, this combination of characteristics defines a wide range of practical applications [4–6]. However, when contact interaction takes place at the microasperity level, many copper alloys exhibit unstable tribological behavior under mixed and unlubricated sliding.

In the absence of lubrication, sliding friction frequently results in the generation of mechanically mixed layers, which subsequently determine the mechanism and intensity of wear under specific load conditions [7, 8]. Targeted modification of the initial microstructure by means of thermal and deformation effects is directly related to the ability to control these processes. Increasing the total grain and twin boundary length, solid-solution strengthening, and dispersion hardening resulting from the precipitation of coherent secondary phases in the matrix are the primary strengthening mechanisms for copper alloys [9].

Interest in solid-state technologies, particularly friction stir welding (*FSW*) and friction stir processing (*FSP*), is growing because traditional fusion welding methods for forming permanent joints in copper and its alloys are often associated with defects and coarse dendritic structures [10, 11].

FSP is a surface modification technique that involves plunging a rotating tool into a workpiece to induce intensive plastic deformation and frictional heating, thereby plasticizing the material without melting it [12, 13]. In this case, the plasticized material flows as a quasi-viscous fluid into the processed zone around the rotating *FSP* tool. A homogeneous, fine-grained, equiaxed grain structure with improved mechanical properties is formed due to layer-by-layer transfer to the zone behind the tool, facilitated by adhesive interaction between the tool and the workpiece in addition to quasi-viscous flow [14, 15].

However, *FSP* can also be considered as a technology for repairing large components damaged by erosion or corrosion [16], including the creation of higher-quality parts for later reinforcement of functional machine components [17, 18].

Even though *FSP* has a much lower peak temperature (~0.4 $\boldsymbol{T_m}$) than fusion welding, it may still have a substantial thermal impact on the workpiece metal. Controlling the temperature field, mainly by altering the *FSP* tool angular speed, is crucial for heat-sensitive alloys that are susceptible to thermal hardening or, conversely, to softening in the heat-affected zone (*HAZ*).

This issue is especially severe for copper alloys because of their high thermal conductivity, which causes the generated heat to be quickly removed from the processed zone, consequently deteriorating the metal's plasticization and interfering with the transfer process [19]. This requires the generation of additional thermal energy, which can be achieved by increasing the tool rotation speed, as mentioned above. In turn, such an increase can result in excessive frictional heating, which would negatively impact weld formation and allow the formation of a heat-affected zone.

To obtain the required structure and properties, forced cooling may be necessary during *FSP*. The workpiece and the tool body should be cooled because friction between the tool shoulder and the workpiece surface is the main cause of heat generation.

To the best of our knowledge, insufficient attention has been paid to the systematic investigation of the impact of the heat removal rate on the properties and structure formation of copper alloys subjected to *FSP*. However, known studies exist that use compressed air, liquid or gaseous nitrogen, carbon dioxide (in liquid or gaseous form or as dry ice), water (by workpiece immersion or directed supply to the contact zone), and other coolants in *FSP* [21–24]. Specifically, *Sedeghati* and *Bouzary* [25] showed that *FSP* of *AA5086* aluminum alloy sheets with water cooling boosted joint tensile strength by 94%. *Behtaripour* et al. [26] demonstrated that an increase in the cooling rate during *FSP* of heat-strengthened *AA2024* aluminum alloy results in improved strength characteristics and grain refinement. *Xu* et al. [27] reported that when brass is actively cooled, nanotwins and dislocation clusters form in the structure, increasing the ultimate tensile strength and yield strength by 24% and 31%, respectively, compared to *FSP* without cooling. Additionally, in another study, *Xu* et al. [28] observed an increase in the tensile strength of the 70/30 brass joint obtained by *FSP* with active cooling, even in the presence of numerous micropores and oxide inclusions.

Based on this, ***the aim of this study*** was to determine how the application of forced cooling techniques (air and water) during single-pass friction stir processing would affect the mechanical properties, grain morphology, and structural and phase state formation of the stirring zone of industrial copper alloys with different elemental compositions and thermal conductivities. The following research ***tasks*** were formulated to accomplish this aim:

– to determine the characteristics of the structural-phase state formation and mechanical properties of copper alloys following single-pass friction stir processing with active water cooling;

– to ascertain how the intensity of active water cooling applied during friction stir processing influences the structural morphology and mechanical properties of aluminum bronze;

– to ascertain the material behavior characteristics of copper alloys during and after friction stir processing with active water cooling and their differences from friction stir processing with air cooling.

Methods

The *FSP* was conducted on an experimental setup created at the *Institute of Strength Physics and Materials Science SB RAS* to investigate the impact of processing modes on the evolution of the structure and properties of metals and alloys within the framework of a thesis work. Plates composed of *Cu-9Al-2Mn*, *Cu-6Sn-P*, *Cu-3Si-1Mn*, and *Cu-37Zn* alloys underwent single-pass *FSP*. A heat-resistant nickel superalloy *ZhS6U FSP* tool with a smooth conical pin having a length of $\boldsymbol{l}$ = 1.9 mm and a shoulder diameter of about 20 mm was used. The *FSP* tool axis inclination angle was 1° with respect to the workpiece normal, counted in the direction opposite to the processing direction. To avoid tool breakage, the alloy plates were reliably clamped to the stainless steel substrate and the working table.

A combined scheme was used to implement forced water cooling: the workpiece was submerged in a bath of flowing water, and **a** coolant was also circulated through the tool casing (water temperature $\boldsymbol{T_{water}}$ = 10–15 °C) (Fig. 1, pos. **1**). Additionally, a tube with an outlet diameter of $\boldsymbol{D}$ = 7 mm was used to supply a directed water stream to the area where the tool made contact with the workpiece ($\boldsymbol{T_{water}}$ = = 2–10 °C, volumetric flow rate $\boldsymbol{V}$ = 13 L/min) (Fig. 1, pos. **2**). Compressed air flowed through a tube with an outlet opening of $\boldsymbol{D}$ = 20 mm to the processed area behind the tool ($\boldsymbol{T_{air}}$ = 35–40 °C, flow rate $\boldsymbol{V}$ = 40 L/min) to provide air cooling.

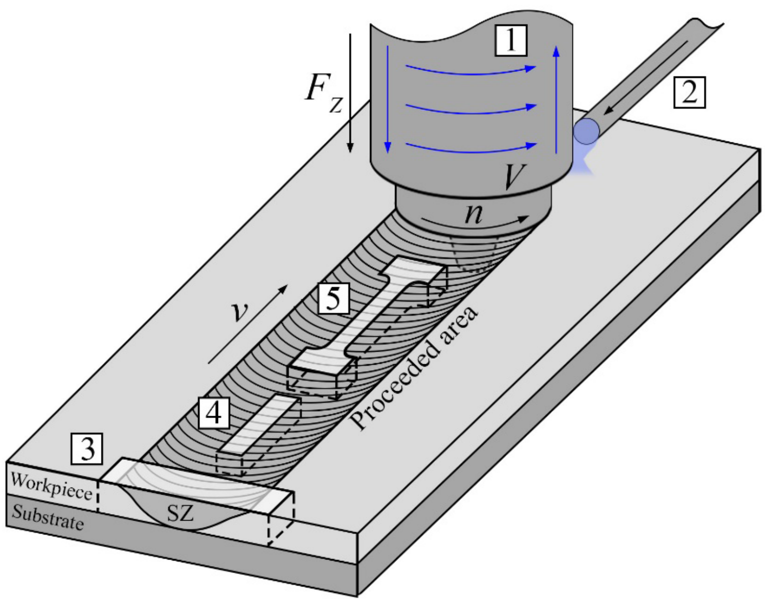

Fig. 1. Schematic representation of friction stir processing (*FSP*) with forced cooling

In every experiment, the worktable with the workpiece had a translational speed in relation to the stationary tool $\boldsymbol{v}$ = 90 mm/min, and the tool rotational speed was $\boldsymbol{n}$ = 500 rpm. Table 1 displays additional process parameters that are different for each alloy, such as axial plunging force $\boldsymbol{F_{pl}}$, axial force during processing $\boldsymbol{F_z}$, and the computed process power $\boldsymbol{P}$.

Table 1

Parameters of friction stir processing

Specimen	Alloy	F_{pl} (kN)	F_z (kN)	P (kW)
Al-1	*Cu-9Al-2Mn*	16.7	15.7	0.91
Al-2		17.7	16.7	0.97
Al-3		19.6	18.6	1.08
Sn-1	*Cu-6Sn-P*	15.7	14.7	0.85
Sn-2		16.7	15.7	0.91
Si-1	*Cu-3Si-1Mn*	23.5	22.6	3.66
Si-2		27.0	26.0	4.21
Zn-1	*Cu-37Zn*	16.7	15.7	1.82
Zn-2		18.6	17.7	2.04
Zn-3		19.6	18.6	2.16

Following the application of plunging force $\boldsymbol{F_{pl}}$ to insert the rotating tool into the workpiece, the torque value and the material resistance force acting on the tool along the weld axis were automatically recorded, while the processing force along the tool axis $\boldsymbol{F_z}$, the tool rotation speed, and the workpiece movement speed were preset. The relationship [29, 30] was used to calculate the power generated in a single processing pass:

$$P = \frac{2}{3}\frac{\mu F_z}{S_{shoulder} + S_{pin}}\omega\left(R^3_{shoulder} + 3R^2_{pin} l_{pin}\right), \quad (1)$$

where $\boldsymbol{\mu}$ is the coefficient of friction between the workpiece and the tool; $\boldsymbol{S_{shoulder}}$ and $\boldsymbol{S_{pin}}$ are the contact areas of the shoulder and pin with the workpiece, respectively; $\boldsymbol{\omega}$ is the angular velocity of the tool rotation; $\boldsymbol{R_{shoulder}}$ and $\boldsymbol{R_{pin}}$ are the radii of the shoulder and pin parts, respectively; $\boldsymbol{l_{pin}}$ is the length of the pin.

Table 1 also includes the computed power values for each specimen.

Based on initial experiments, the entire set of processing parameters was chosen to guarantee the best conditions for mechanical stirring of plasticized metal to produce flawless welds. Since the presence of a water layer made it difficult to use thermal imaging equipment, temperature measurements in the mixing zone did not appear to be necessary. Additionally, the use of thermocouples was not anticipated due to potential disruptions to the material transfer process and defect formation.

Criteria and heat removal

The rate of heat removal from the processed surface to the coolant was estimated using the *Newton–Richmann* law:

$$q = \alpha S_{pr}\left(T_2 - T_1\right), \quad (2)$$

where $\boldsymbol{S_{pr}}$ is the area of the heat-transferring surface; $\boldsymbol{T_2}$ is the temperature of the treated surface; $\boldsymbol{T_1}$ is the temperature of the coolant; $\boldsymbol{\alpha}$ is the heat transfer coefficient, defined as:

$$\alpha = \frac{Nu \cdot \lambda}{D}, \quad (3)$$

where$\boldsymbol{\lambda}$ is the thermal conductivity of the coolant; $\boldsymbol{D}$ is the diameter of the nozzle outlet section; $\boldsymbol{Nu}$ is the *Nusselt* number.

For forced convection conditions with turbulent impact flow from a round nozzle, the *Nusselt* number was calculated using the criterial relationship [31, 32]:

$$Nu = C \cdot \mathrm{Re}^m \cdot \mathrm{Pr}^n, \tag{4}$$

where $\boldsymbol{C}$ = 0.76, $\boldsymbol{m}$ = 0.6, $\boldsymbol{n}$ = 0.4; $\boldsymbol{Pr}$ is the *Prandtl* number (for air at 30 °C, $\boldsymbol{Pr}$ = 0.7; for water at 10 °C, $\boldsymbol{Pr}$ = 9.45); $\boldsymbol{Re}$ is the *Reynolds* number:

$$Re = \frac{V \cdot D \cos\theta}{S_{nozzle} \nu}, \tag{5}$$

where $\boldsymbol{V}$ is the volumetric flow rate of the coolant; $\boldsymbol{\theta}$ is the jet angle to the surface; $\boldsymbol{S_{nozzle}}$ is the outlet cross-sectional area; $\boldsymbol{\nu}$ is the kinematic viscosity of the coolant.

To evaluate the effect of heat removal intensity on the mechanical properties, a series of *Cu-9Al-2Mn* aluminum bronze specimens was used, the *FSP* parameters of which are presented in Table 2.

Table 2

Characteristics of specimens for evaluation of cooling intensity

Specimen	Alloy	F_{pl} (kN)	F_z (kN)	Cooling	V (L/min)	q (kJ/s)
Al-4	*Cu-9Al-2Mn*	15.2	13.2	air	40	0.16
Al-5				water	7	29.8
Al-6					13	43.2
Al-7					20	55.9

Specimens preparation and equipment

A *YXLON Cheetah EVO* X-ray inspection system (*Comet Yxlon*, Germany) was used to inspect the processed workpieces prior to cutting out the specimens in order to identify the specimen cutting location free of macrodefects and foreign particles, such as substrate fragments mixed into the stir zone when the tool penetrated too deeply. A *DK7750* electrical discharge machine (*Suzhou Simos CNC Technology Co. Ltd.*, China) was used to cut off specimens of two orientations from the processed workpieces: 20 mm × 5 mm transverse sections for microhardness measurements and metallographic analysis (Fig. 1, pos. **3**); longitudinal specimens in the form of cylindrical columns with a cross-section of 3 mm × 10 mm for tribological testing utilizing the "pin-on-disk" scheme (Fig. 1, pos. **4**); and specimens for uniaxial tension with the gauge part measuring 12 mm × 3 mm (Fig. 1, pos. **5**).

The transverse sections' surfaces were first ground with 180 to 2,000 µm abrasive paper, polished with 1/0 µm diamond paste, and finally chemically etched in a solution consisting of 10 mL *HCl* + 1 g $FeCl_3$ + + 20 mL H_2O. An *Altami MET 1C* optical microscope (*Altami LLC*, Russia), an *Olympus LEXT OLS4100* laser confocal scanning microscope (*Olympus Corporation*, Japan), and a *Carl Zeiss LEO EVO 50* scanning electron microscope (*SEM*) (*Carl Zeiss AG*, Germany) with an energy-dispersive X-ray spectroscopy (*EDS*) attachment (Oxford Instruments, UK) were used to examine the microstructure. Using metallographic images of cross-sections, the linear intercept method was used to calculate the average grain size.

A *UTS 110M-100* universal tensile testing machine (*Testsystems*, Russia) was used to conduct uniaxial static tensile testing at a crosshead speed of 1 mm/min. A *TBM 5215A Tochline* instrument (*Tochpribor*, Russia) was used to record microhardness profiles in 0.5 mm increments along a line that was equally spaced from the treated area and the root face under a load of 4.9 N and a hold time of 10 s.

Results and discussion

Aluminum bronze Cu-9Al-2Mn

Following *FSP*, cross-sectional analysis of *Cu-9Al-2Mn* aluminum bronze specimens showed pinpoint discontinuities within the stir zone (*SZ*) and localized thermal damage on the weld face. The lower part of the *SZ* was characterized by mechanically mixed transition layers, intermetallic inclusions, and embedded substrate material fragments (Fig. 2, *a*–*c*, pos. **3**), brought on by the occurrence of vertical tool endplay. Because of the workpiece's high plasticization and excessive adhesion to the tool's working surface, tool material transfer into the *SZ* remained negligible. The majority of discontinuities were found in the subsurface areas of the *SZ*, close to large inclusions of the substrate material, and close to the interface with the substrate (Fig. 2,*a*–*c*, pos. **2**). Specimen *Al-2* ($\boldsymbol{F_{pl}}$ = 16.7 kN) had the highest defect density (Fig. 2, *b*), whereas specimen *Al-1* ($\boldsymbol{F_z}$ = 15.7 kN) had few defects and a low level of embedded substrate material.

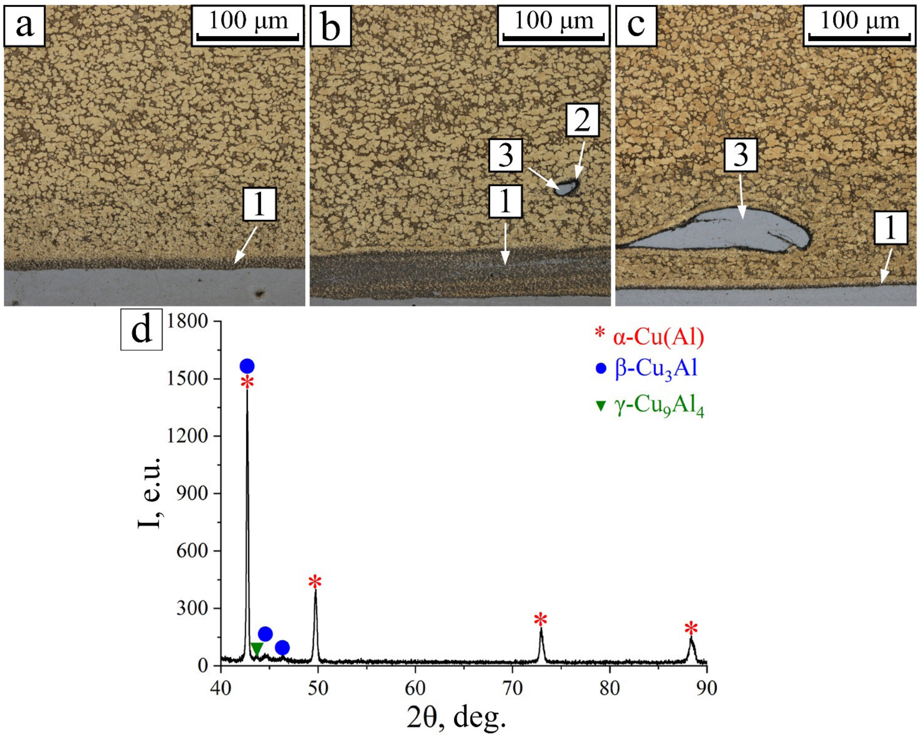

Fig. 2. Optical micrographs of macrostructure (*a*–*c*), and X-ray diffraction pattern (*d*) of specimens ***Al-1*** (*a*, *d*), ***Al-2*** (*b*), and ***Al-3*** (*c*)

X-ray phase analysis findings (Fig. 2, *d*) show the formation of the $\boldsymbol{\gamma_2}$-Cu_9A_4 phase, which is indicative of the eutectoid decomposition of **β**-Cu_3Al according to the $\boldsymbol{\beta \rightarrow \alpha + \gamma_2}$ scheme at a temperature of roughly 565 °C, and an increase in the volume fraction of the **β**-Cu_3Al intermetallic phase relative to the prior state. The processed specimens showed a shoulder-driven stir zone (*SSZ*) created by the rotation of the tool shoulder. Because of the shoulder's rotation, the metal in this zone has **β**-Cu_3Al grains that are elongated along the metal flow direction.

Equiaxed grains of the **α**-*Cu(Al)* solid solution, which are smaller than the irregularly shaped grains in the remaining portion of the weld, can be seen closer to the top of the weld and mostly on the advancing side of the weld. The bronze's average grain size was 77 ± 7 µm in its as-received state. The average grain sizes in the *SZ* of specimens *Al-1*, *Al-2*, and *Al-3* were 5.1 ± 0.9, 5.7 ± 0.9, and 5.4 ± 0.7 µm, respectively (Fig. 2, *a*–*c*).

Unwanted tool penetration into the substrate, the capture of stainless steel, and an increase in the width of the transition layer at the substrate boundary from 9.5 to 38 µm were all associated with an increase in the plunging force $\boldsymbol{F_{pl}}$ from 15.7 to 16.7 kN (Fig. 2,*a*, *b*, pos. **1**). The transition layer narrowed to 5.3 µm when $\boldsymbol{F_{pl}}$ was increased further to 18.6 kN (Fig. 2,*c*, pos**. 1**), but this also increased the tool's penetration depth into the substrate, the amount of substrate material intermixed with the SZ (Fig. 2,*c*, pos. **3**), as well as the extent to which the tool-driven displacement of the workpiece material resulted in a reduction in the *SZ* height. *EDS* mapping verified that elements belonging to the bronze composition predominated in the transition layers (Fig. 3).

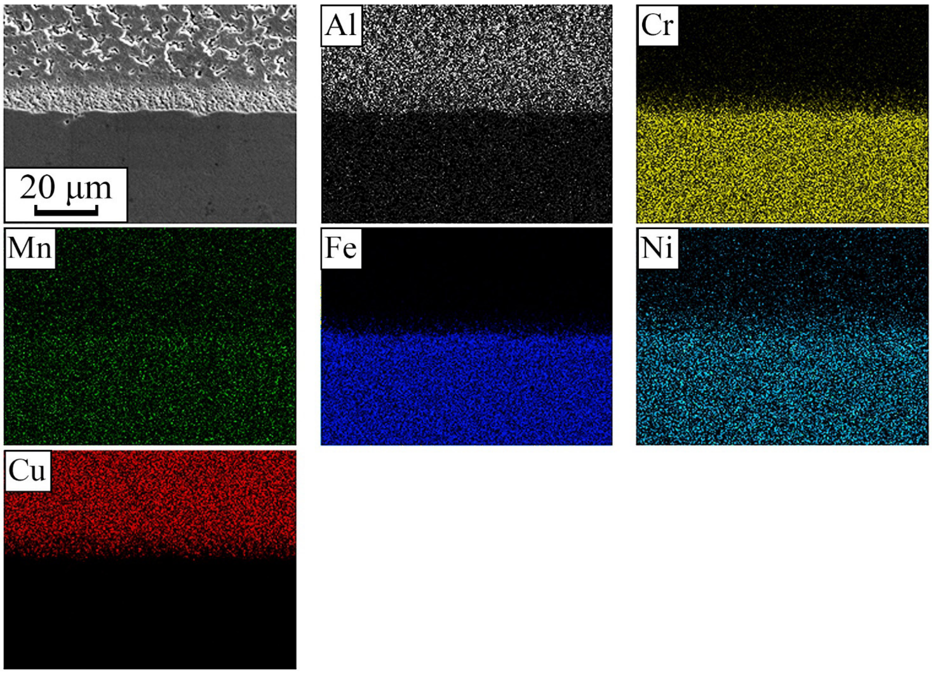

Fig. 3. SEM image of the lower part of the stir zone in specimen ***Al-1*** with a transition layer and *EDS* elemental distribution maps

Enhanced tool rigidity with regard to vertical bending and the use of a helical profile working shoulder at an inclination angle of less than **1°** from the normal to the workpiece surface are necessary to decrease the thickness of the transition layer. As F_{pl} increased, the *SSZ* height stayed essentially constant, the *SZ* width shrank, and the thermomechanically affected zone (*TMAZ*) width expanded, mostly on the retreating side (Fig. 2, *a–c*). The microstructure of the *TMAZ* is similar to that of the base metal, but it contains more **β**-Cu_3Al, as well as grains elongated by plastic flow. An increase in its width with increasing axial force is thought to be harmful to the full strength of the joint because the *TMAZ* in copper alloys is usually a weakened zone and has lower hardness than the *SZ*.

Specimens *Al-1*, *Al-2*, and *Al-3* had *SZ* microhardness levels that were 6.3, 3.8, and 7.1% higher than the starting level, respectively (Fig. 4, *b*), which is probably the result of *Hall-Petch* strengthening provided that the size of recrystallized grains decreased significantly. The ultimate tensile strength (*UTS*) of these specimens increased by 11, 12, and 12%, respectively, according to quasi-static uniaxial tensile tests. Concurrently, the yield strength (*YS*) values dropped by 28, 25, and 20% (Fig. 4).

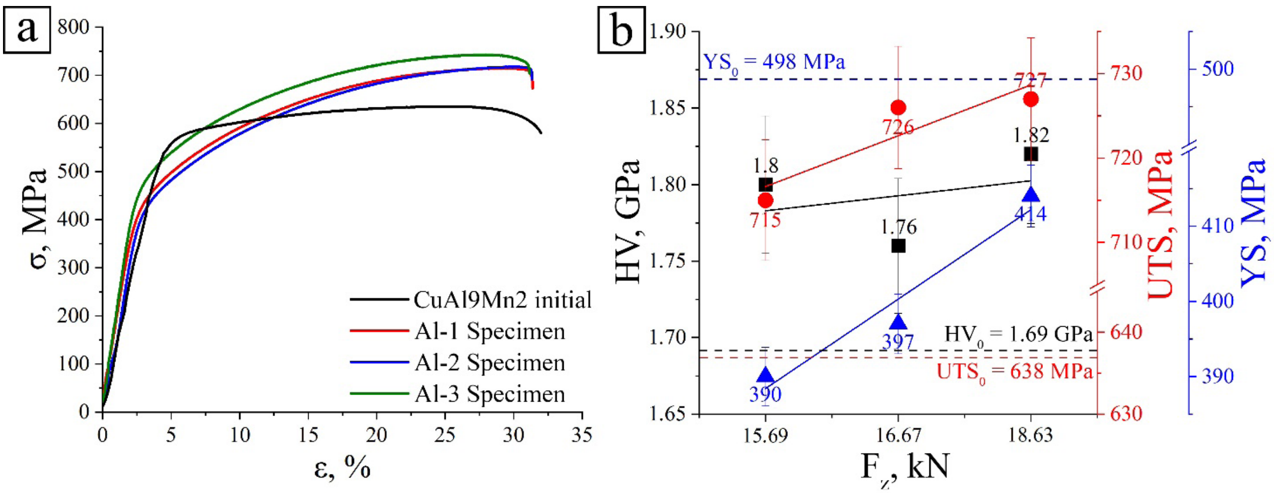

Fig. 4. (*a*) Stress-strain curves and (*b*) mechanical properties of specimens ***Al-1***, ***Al-2***, and ***Al-3***

Tin Bronze Cu-6Sn-P

In contrast to *Cu-9Al-2Mn*, the stir zone of a *FSP*ed tin bronze *Cu-6Sn-P* does not contain significant tool-mixed substrate fragments, although there is some stainless steel mixing into the root area (Fig. 5). Delamination defects were observed at the *SZ* boundary on the retreating side between the transferred material layers; these were most noticeable in specimen *Sn-2* ($\boldsymbol{F_0}$ = 14.7 kN) (Fig. 5,*b*, pos. **1**.). An "onion ring" structure consisting of alternating concentric layers typical of the *SZ* nugget was formed by *FSP*. Specimens *Sn-1* and *Sn-2* had average grain sizes of 5.5 ± 1.5 and 7.7 ± 3.1 μm, respectively. In addition, no *TMAZ* is observed, in contrast to the *HAZ*, which is evidently present.

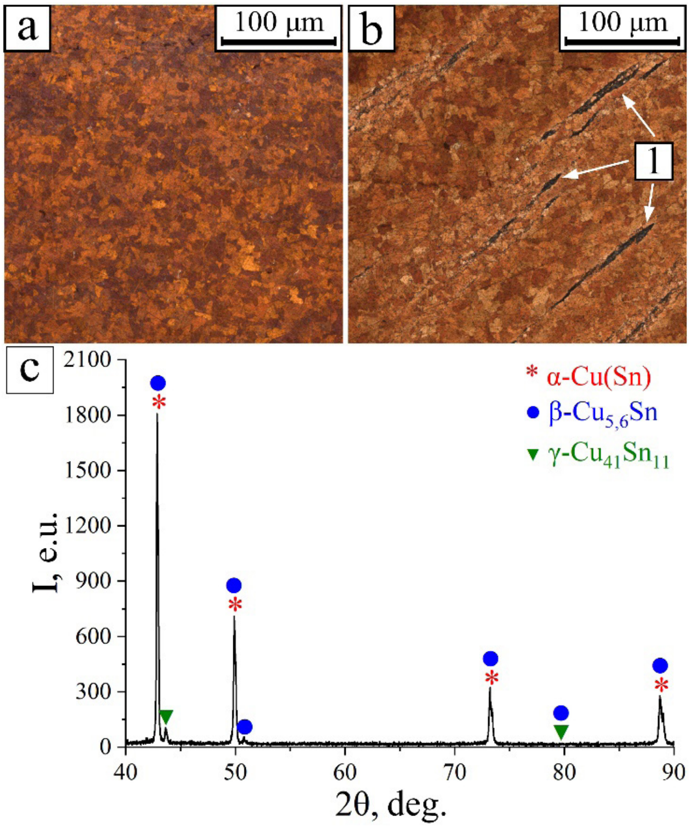

Fig. 5. (*a*, *b*) Optical images of macrostructure and (*c*) X-ray diffraction pattern of specimens ***Sn-1*** (*a*) and ***Sn-2*** (*b*, *c*)

This type of structural evolution is typical of copper alloys subjected to *FSP*. It should be noted that in order to form a clearly visible *TMAZ* zone, a considerable percentage of secondary phase grains and intermetallic inclusions should appear in it in addition to the fine deformed grains. This usually happens because the intensity of deformation-induced particle dissolution in this zone is lower than that in the intensively stirred *SZ*.

X-ray phase examination (Fig. 5,*c*) enabled us to detect the existence of such phases as **β**-$Cu_{5.6}Sn$ and metastable **γ**-$Cu_{41}Sn_{11}$ in addition to the original **α**-*Cu(Sn)* solid solution. The peritectic reaction ***L*** + **α**-*Cu* is capable of forming this bcc phase **β**-$Cu_{5.6}Sn$ in the temperature range of 586–798 °C, which then decomposes upon further cooling according to the reaction **β** → **α**-*Cu* + **γ**. Conversely, at 520 **°C**, the reaction **γ** → *Cu* + **ε**-Cu_3Sn serves for further decomposition.

In comparison to the original bronze, the average microhardness level in the SZ decreased by 5.9 and 9.0%, respectively, when the axial plunging force $\boldsymbol{F_{pl}}$ increased from 14.7 kN (*Sn-1*) to 15.7 kN (*Sn-2*) (Fig. 6, *b*), but the microhardness number scatter across the *SZ* width also decreased. After *FSP*, both tensile strength and yield strength dropped: UTS dropped by 1.58 and 1.60 times, *YS* by factors of 2.4 and 2.5 for *Sn-1* and *Sn-2*, respectively, while the relative elongation increased by factors of 3.3 and 3.5 (Fig. 6).

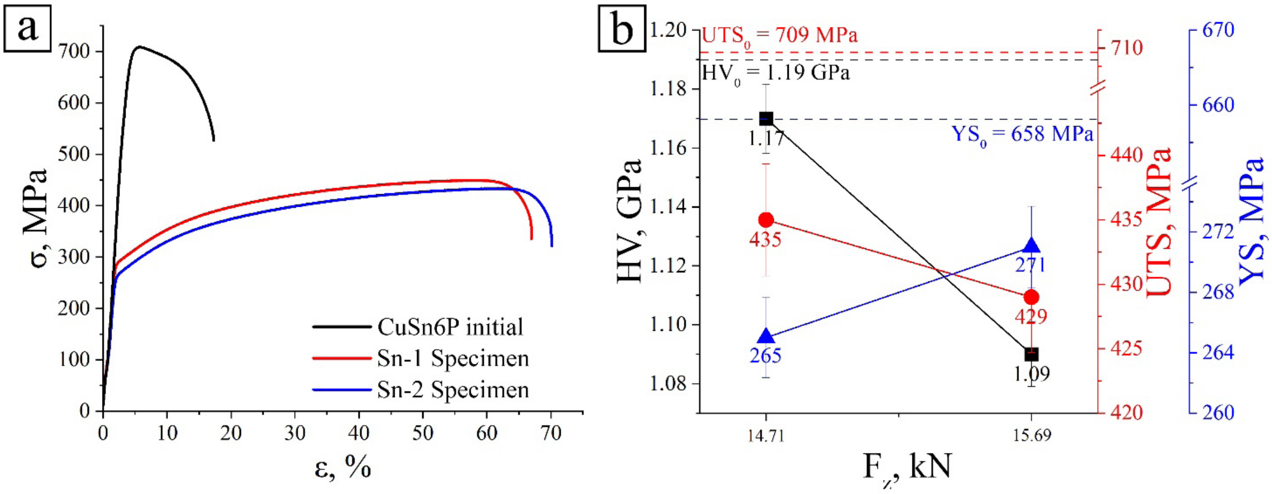

Fig. 6. (*a*) Stress-strain curves and (*b*) mechanical properties of specimens ***Sn-1*** and ***Sn-2***

Such behavior may be brought on by overaging of intermetallic phases relative to the initial as-received condition, as well as by softening brought on by grain recrystallization (elimination of work hardening).

Silicon-manganese bronze Cu-3Si-1Mn

FSP on *Cu-3Si-1Mn* silicon-manganese bronze produced grains with an average longitudinal size of 409 ± 82 μm, which was larger than their size in the transverse direction. Following processing at F_{pl} = 22.6 and 26.0 kN (specimens *Si-1* and *Si-2*), their shape approached equiaxed and their average grain size dropped to 16 ± 6 and 17 ± 6 μm, respectively (Fig. 7, *a*, *b*). Similar to *Cu-6Sn-P*, the specimens

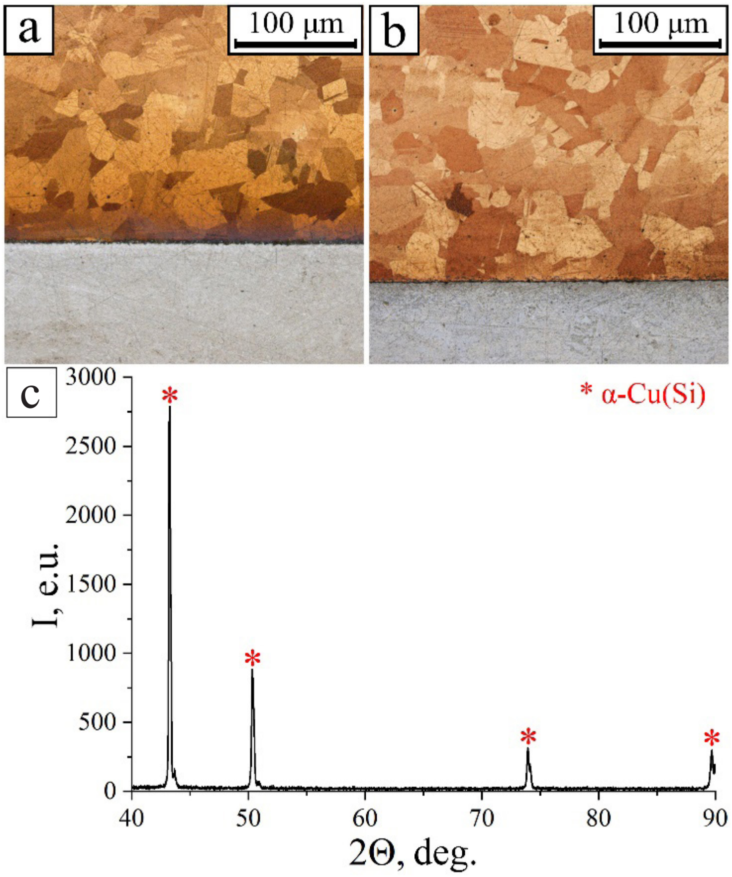

Fig. 7. (*a*, *b*) Optical micrographs of macrostructure and (*c*) X-ray diffraction pattern of specimens ***Si-1*** (*a*) and ***Si-2*** (*b*, *c*)

of this alloy showed a distinct *HAZ* with intermediate-sized grains, but there was no discernible *TMAZ*. According to X-ray phase analysis, the structure is represented by **α**-*Cu*(*Mn*) solid solution (Fig. 7, *c*) with a silicon content of approximately 2.9 wt.%. Based on the *Cu-Si* equilibrium diagram, the formation of any intermetallic phases with this composition is unlikely.

A discernible softening of the stir zone material was another outcome of the *FSP* of *Cu-3Si-1Mn* silicon-manganese bronze. The microhardness values for *Si-1* and *Si-2* were 0.98 and 1.07 GPa, respectively, whereas initial microhardness in the as-received metal of 1.73 GPa. Tensile and yield strengths decreased from 605 MPa and 552 MPa to 410–413 MPa and to 205– 200 MPa, respectively (Fig. 8). Grain coarsening and a decrease in dislocation density [33] brought on by the dynamic recrystallization typical of *FSP* conditions explain the observed decline of mechanical properties.

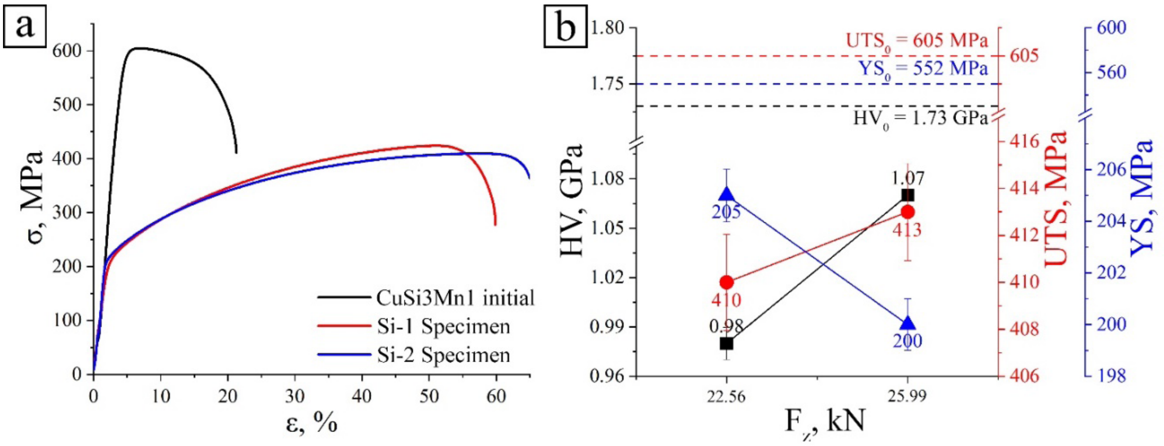

Fig. 8. (*a*) Stress-strain curves and (*b*) mechanical properties of specimens ***Si-1*** and ***Si-2***

Brass Cu-37Zn

Elongated grains with a longitudinal size of 217 ± 43 μm were the hallmark of the original dual-phase brass *Cu-37Zn*. The grain sizes in specimens *Zn-1*, *Zn-2*, and *Zn-3* ($\boldsymbol{F_{pl}}$ = 15.7, 17.7, and 18.6 kN) reduced to 2.8 ± 0.4, 3.3 ± 0.5, and 3.3 ± 0.4 μm, respectively, due to severe plastic deformation and dynamic re-crystallization (Fig. 9, *a*–*c*). The macrostructure revealed a *TMAZ* with refined grains elongated along the *SZ* in the direction of material flow.

In addition to the **α**-*Cu(Zn)* solid solution, the *XRD* pattern **revealed** (Fig. 9,*d*) the presence of the $Cu_{0.64}Zn_{0.36}$ phase, which is evidence of **β**-*CuZn* decomposition upon cooling below 454 °C**.**

As a result of grain boundary strengthening, the microhardness of samples *Zn-1*, *Zn-2*, and *Zn-3* increased by 28, 30, and 26% (Fig. 10,*b*), as did the ultimate tensile strength by 3.7, 3.4, and 3.5%**,** respectively (Fig. 10). The *Portevin–Le Chatelier* discontinuous yield effect was noted at the strain-hardening stages of the tensile curves for all specimens, as a manifestation of the dynamic aging phenomenon (Fig. 10, *a*).

Strain behavior of copper alloys in FSP

An intricate pattern of stress distribution, temperature and strain rate gradients, quasi-viscous flow, and adhesive transfer are characteristics of the tool-workpiece metal interaction during *FSP*. The tool is surrounded by a layer of plasticized metal that undergoes severe plastic deformation, which is equivalent to a strain **ε** = 9–30 [34]. Layer-by-layer extrusion flow combined with adhesion-mediated transfer along the tool contour is the main transfer mechanism. The original grains undergo deformation-induced segmentation, dynamic recrystallization, loss of shear stability, and transfer to the region behind the tool. Tool wear may result from this intensive diffusion interaction between the plasticized metal and the tool material [35]. The plasticized material stops flowing when it is transferred to the space behind the tool, adheres to the preceding layer, and then experiences final (now static) recrystallization and grain growth. The size of the recrystallized grains increases to the micrometer scale due to intense heat exposure, and only numerical modeling techniques can accurately assess the equivalent deformation [34].

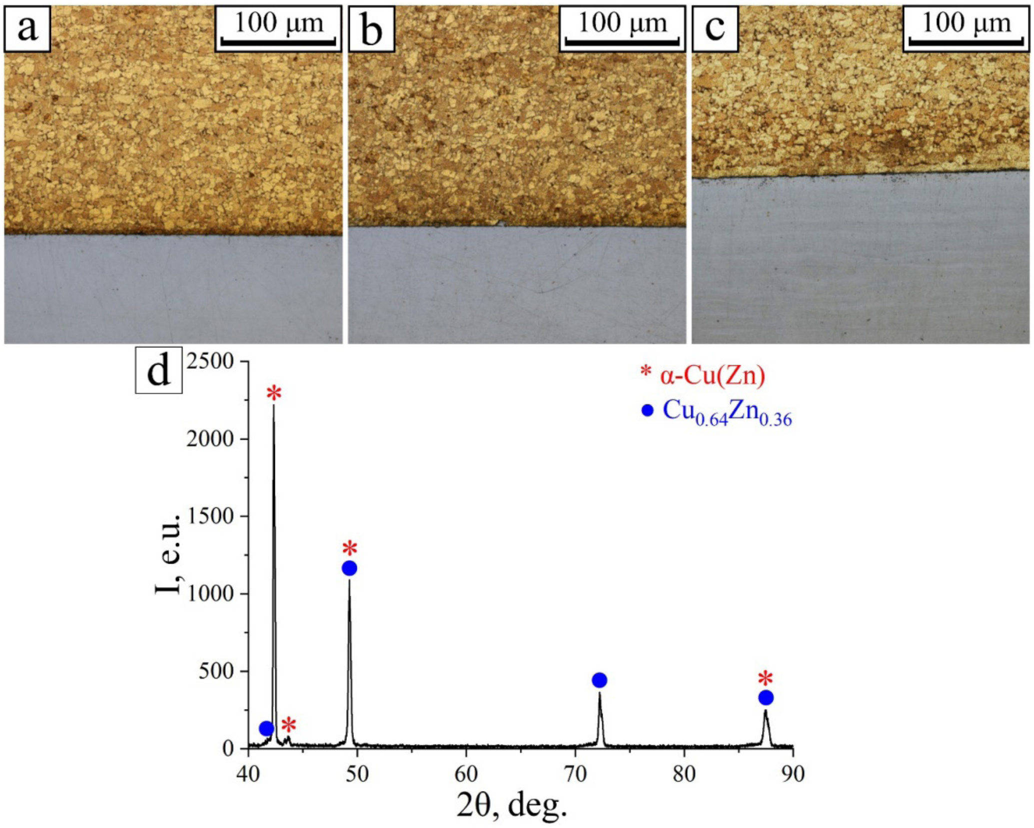

Fig. 9. (*a–c*) Optical micrographs of macrostructure and (*d*) X-ray diffraction pattern of specimens ***Zn-1*** (*a*), ***Zn-2*** (*b*), and ***Zn-3*** (*c*, *d*)

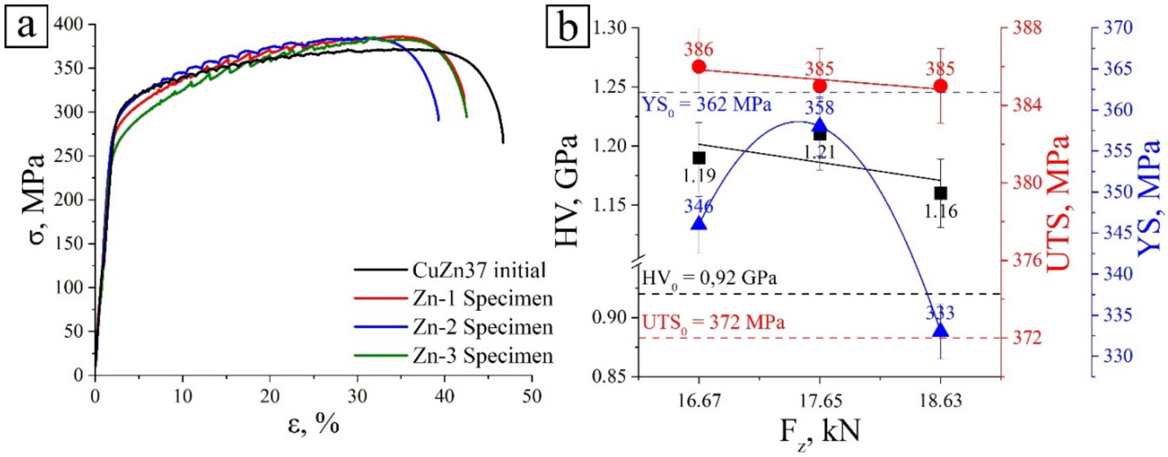

Fig. 10. (*a*) Stress-strain curves and (*b*) mechanical properties of specimens ***Zn-1***, ***Zn-2***, and ***Zn-3***

Copper alloys are fundamentally different from other structural materials in their high thermal conductivity, which provides quick heat removal and temperature equalizing throughout the workpiece and interferes with thermally activated processes like secondary phase precipitation and dynamic recrystallization. This is demonstrated by the distinctive formation of the *SZ*, the width of which remains equal to the tool shoulder diameter over almost the whole workpiece thickness. Additionally, the material flow lines characteristic of titanium and aluminum alloys (Fig. 11, *a*) are typically not discernible in copper alloys (Fig. 11, *b*). The typical "onion ring" morphology (Fig. 11, *a*, pos. 2), the split into pin-driven (Fig. 11,*a*, pos. **1**) and shoulder-driven stir zones (Fig. 11, *a*, pos. 3), as well as the development of a large thermomechanically affected zone (Fig. 11, *a*, pos. 4), are of rare occurrence. Only *Cu-6Sn-P FSP*ed specimens showed the flow line pattern among the materials under investigation. Additionally, layer-by-layer extrusion flow around the tool is facilitated by the high ductility of copper alloys (Fig. 11, *b*).

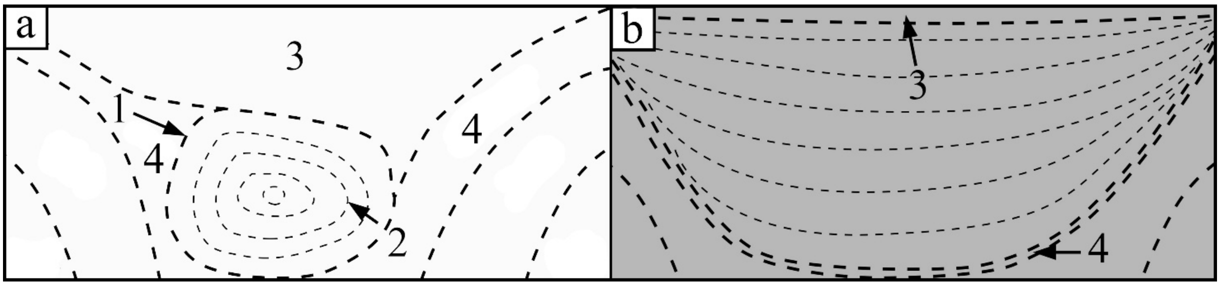

Fig. 11. Comparative schematic of structure formation in (*a*) aluminum alloys and (*b*) copper alloys after friction stir processing

The role of heat dissipation intensity (using the Cu-9Al-2Mn as an example)

The impact of the heat removal rate on the behavior of specimens *Al-4–Al-7* (Table 2) has been assessed in a series of experiments. It was discovered that an increase in the heat removal rate during *FSP* was accompanied by a decrease in the level of mechanical properties, particularly in tensile strength and ductility, even though the treated material was somewhat stronger than the original bronze. After *FSP* with air flow cooling, specimen *Al-4* reached the maximum yield stress *YS* = 559 MPa. For specimen *Al-7* (Fig. 12), the switch to water cooling (*Al-5*) resulted in a *YS* decrease to 475 MPa, but the subsequent increase in water flow rate and, consequently, the heat removal rate caused a gradual increase in the yield strength to 520 MPa.

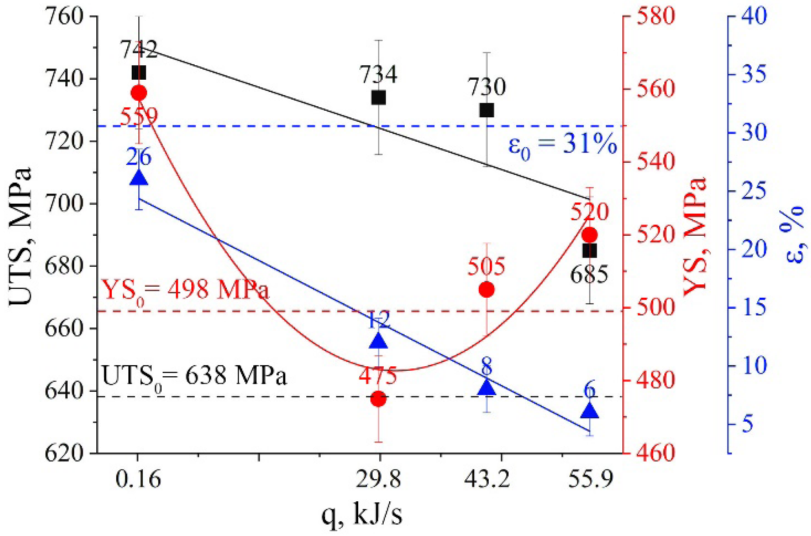

Fig. 12. Dependence of mechanical properties of the *Cu-9Al-2Mn* alloy on cooling intensity during friction stir processing

The impact of thermal conductivity and cooling mode on grain structure

Reduced axial force encourages the formation of defects in the stir zone because copper alloys have a high thermal conductivity combined with workpiece thicknesses of 2–2.5 mm. In order to avoid this, $\boldsymbol{F_{pl}}$ must be raised, and the transition from air to water cooling necessitates an additional increase in the axial force by 19% for *Cu-6Sn-P*, 24% for *Cu-37Zn*, and 111% for *Cu-9Al-2Mn*. When *FSP* is combined with air cooling, either a thin, hardly visible shoulder stir zone (*SSZ*) forms there or it does not form completely (Fig. 13, ***a***, *b*, pos. **1**) as a result of the plasticized metal's slow cooling. In contrast, water cooling causes a pronounced differentiation of grain morphology in the conventional upper (Fig. 13, *d*, pos. **1**), middle (Fig. 13, *d*, pos. **2**), and lower (Fig. 13, *d*, pos. **3**) parts of the *SZ*.

Because copper alloys undergo plastic deformation during *FSP*, the occurrence of dynamic recrystallization is sensitive to the stacking fault energy (*SFE*) level. Therefore, *Cu-9Al-2Mn*, *Cu-6Sn-P*, and *Cu-3Si-1Mn*

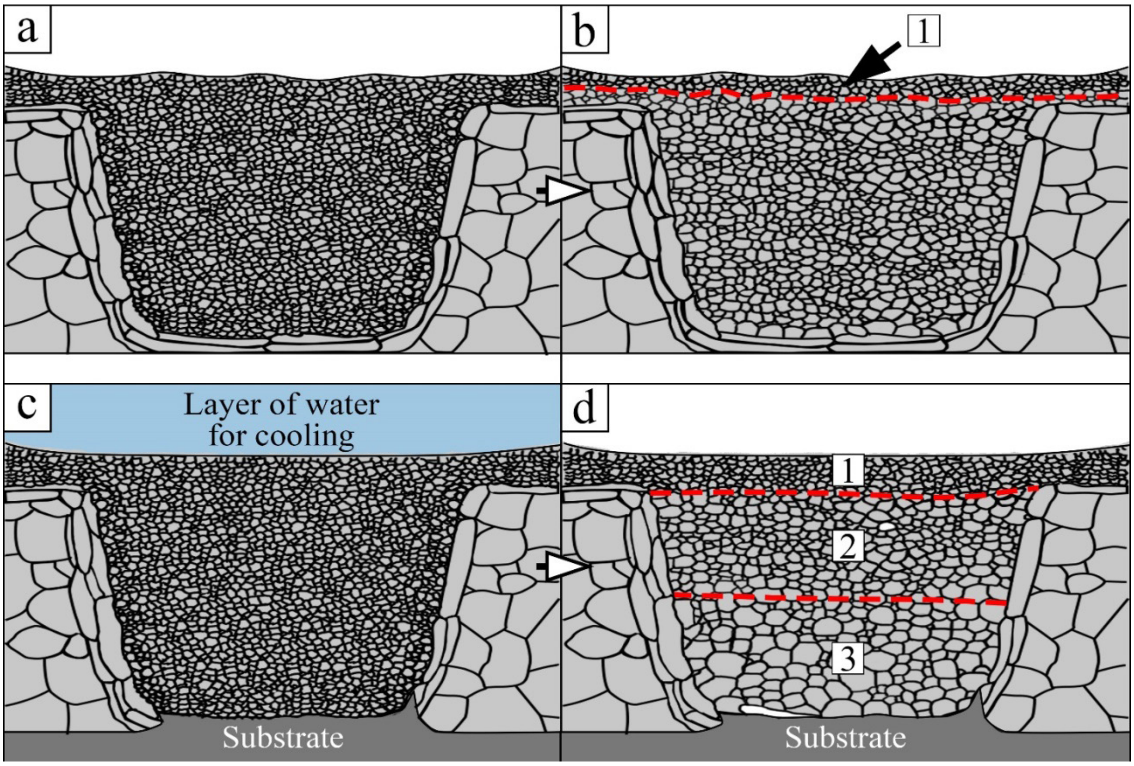

Fig. 13. Schematic of grain structure evolution in copper alloys during *FSP* with (*a*, *b*) air cooling and (*c*, *d*) water cooling: during recrystallization (*a*, *c*); after its completion (*b*, *d*)

bronzes with reduced *SFE* are characterized by a predominance of discontinuous dynamic recrystallization (*DDR*) due to the high density of non-annihilated dislocations, even though the recrystallization mechanism for all copper alloys was generally of a mixed nature. *DDR* results in the formation of a non-homogeneous grain-size structure. Consequently, a more size-homogeneous ultrafine-grained structure is guaranteed in the brass because of its higher *SFE* [36, 37].

Intense water cooling of the weld face during static recrystallization inhibits the growth of recrystallized grains in the upper part of the *SZ*, leading to the formation of an *SSZ* with a finer-grained structure. On the other hand, slow heat removal provokes the growth of recrystallized grains in the *FSP*ed root zone. This effect is most noticeable in alloys with a lower thermal conductivity coefficient (λ), which results in less uniform cooling of the processed volume. This gradient is less noticeable in alloys with higher thermal conductivity, but the presence of embedded substrate material at the weld root further slows recrystallization, increasing the local grain size (Fig. 14, *d*). This effect outweighs the effects of *SFE* and the type of recrystallization in specimens that have undergone *FSP*. The dependence of grain size ***d*** on the alloys' thermal conductivity coefficient **λ** quantitatively reflects this trend: in water-cooled specimens, an increase in **λ** is accompanied by a decrease in grain size ***d*** in the middle and lower parts of the *SZ* (Fig. 14, *b*, zones **2**, **3**); high thermal conductivity and air cooling also cause grain refinement, primarily in the upper *SZ* (Fig. 14, *a*). This also accounts for the yield strength's non-monotonic dependence on the heat removal rate, which was observed when varying the cooling intensity (Fig. 11).

Conclusion

The following was determined after a thorough investigation of the effects of single-pass friction stir processing with forced cooling by air and water flows on the mechanical properties and structural-phase state of industrial copper alloys *Cu-9Al-2Mn*, *Cu-6Sn-P*, *Cu-3Si-1Mn*, and *Cu-37Zn*:

1. *FSP* guarantees the formation of a recrystallized fine-grained structure with primarily equiaxed grains in all the alloys under study. The microhardness *HV* and tensile strength *UTS* of *Cu-37Zn* brass specimens increased to 1.82 GPa and 727 MPa in *Cu-9Al-2Mn*, thus exceeding the original bronze's characteristics by

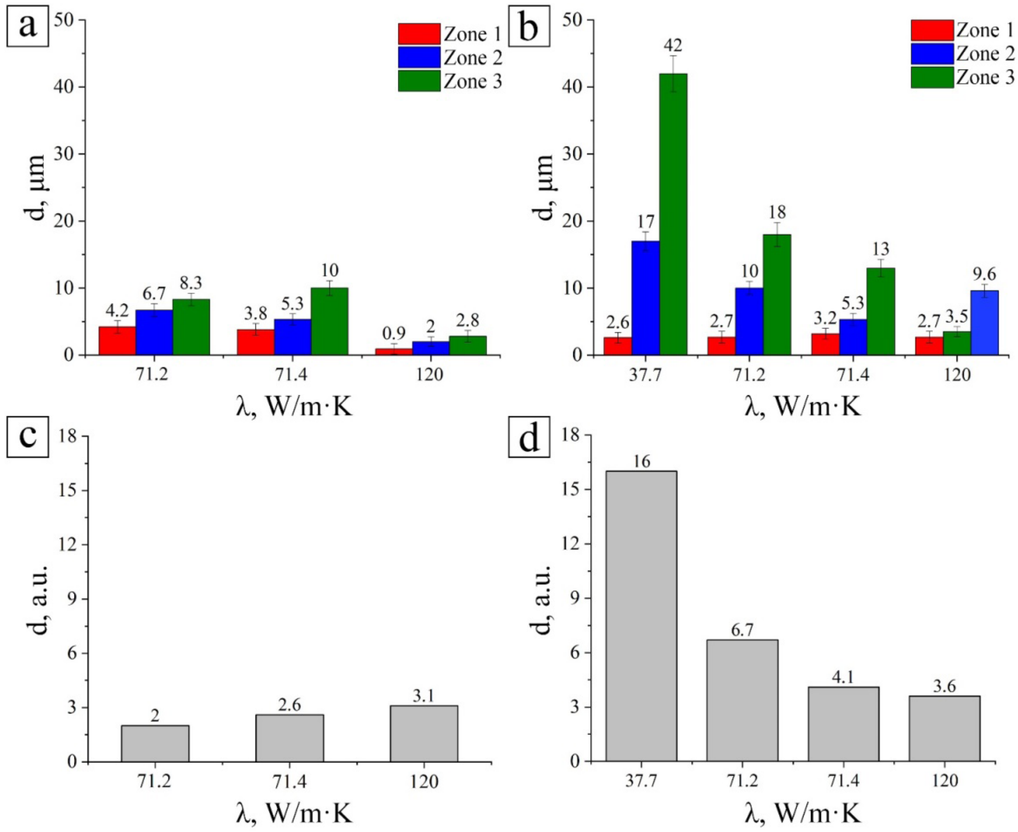

Fig. 14. (*a*, *b*) Grain size dependence on the thermal conductivity of the alloys and (*c*, *d*) relative grain size variation along the stir zone height after *FSP* with (*a*, *c*) air cooling and (*b*, *d*) water cooling

7 and 12%, respectively. The same characteristics exceeded those of the original *Cu-37Zn* brass by 22 and 4% and reached 1.19 GPa and 386 MPa, respectively.

2. Changing the intensity of active water cooling during *FSP* resulted in a gradual decrease in ductility (from 12% to 6%) and ultimate strength (from 734 to 685 MPa) of the *FSP*ed specimens, as well as an increase in their yield strength (from 475 to 520 MPa). However, *FSP* with air cooling (low heat removal rate) resulted in the highest yield strength (559 MPa).

3. *FSP* with air cooling was found to result in a more homogeneous grain size distribution in the *SZ* compared to that exhibited by *FSP* with water cooling, after which a clear non-homogeneous grain size distribution was observed across the *SZ* thickness. The grains are 4–16 times larger in the root part of the *SZ* than those below the weld face surface (*SSZ*). This type of grain size distribution is most clearly seen after *FSP* with water cooling on *Cu-3Si-1Mn* bronze, which has the lowest thermal conductivity (**λ** = 37.7 W/(m·K)). The physical reason is the presence of a temperature gradient and, therefore, a different growth rate of the recrystallized grains: at the cooled weld surface, grain growth is rapidly halted, while at the root it continues, solely because of insufficient heat removal. The increased thermal conductivity of copper alloys is therefore a factor that contributes to the formation of a homogeneous grain size structure in the stir zone, particularly in the case of processing without the use of forced cooling.

References

1. Hamidah I., Solehudin A., Hamdani A., Hasanah L., Khairurrijal K., Kurniawan T., Mamat R., Maryanti R., Nandiyanto A.B.D., Hammouti B. Corrosion of copper alloys in KOH, NaOH, NaCl, and HCl electrolyte solutions and its impact to the mechanical properties. *Alexandria Engineering Journal*, 2021, vol. 60 (2), pp. 2235–2243. DOI: 10.1016/j.aej.2020.12.027.

2. Achiţei D.C., Vizureanu P., Minea A.A., Abdullah M.M.A.B., Minciună M.G., Sandu A.V. Improvement of properties of aluminum bronze $CuAl_7Mn_3$ by heat treatments. *Applied Mechanics and Materials*, 2014, vol. 657, pp. 412–416. DOI: 10.4028/www.scientific.net/AMM.657.412.

3. Lu T., Chen C., Li P., Zhang Ch., Han W., Zhou Y., Suryanarayana Ch., Gou Zh. Enhanced mechanical and electrical properties of in situ synthesized nano-tungsten dispersion-strengthened copper alloy. *Materials Science and Engineering: A*, 2021, vol. 799, p. 140161. DOI: 10.1016/j.msea.2020.140161.

4. Osipovich K., Vorontsov A., Chumaevskii A., Moskvichev E., Zakharevich I., Dobrovolsky A., Sudarikov A., Zykova A., Rubtsov V., Kolubaev E. Features of microstructure and texture formation of large-sized blocks of C11000 copper produced by electron beam wire-feed additive technology. *Materials*, 2022, vol. 15 (3), pp. 814–832. DOI: 10.3390/ma15030814.

5. Tian F., Wu Ch., Zhu B., Wang L., Liu Y., Zhang Y. Research of microstructure, friction and wear on siliconized aluminum-bronze with different silicon powder ratio. *Frontiers in Materials*, 2021, vol. 7, p. 620500. DOI: 10.3389/fmats.2020.620500.

6. Ferreira L.F.P., Bayraktar E., Miskioglu I. Design of hybrid composites from scrap aluminum bronze chips. *Mechanics of Composite and Multi-functional Materials*, 2017, vol. 7, pp. 131–138. DOI: 10.1007/978-3-319-41766-0_15.

7. Schell J., Heilmann P., Rigney D.A. Friction and wear of Cu–Ni alloys. *Wear*, 1982, vol. 75, pp. 205–220. DOI: 10.1016/0043-1648(82)90149-1.

8. Venkataraman B., Sundararajan G. The sliding wear behaviour of Al–SiC particulate composites. II. The characterization of subsurface deformation and correlation with wear behavior. *Acta Materialia*, 1996, vol. 44, pp. 461–473. DOI: 10.1016/1359-6454(95)00218-9.

9. Yang L., Jiang X., Sun H., Shao Zh., Fang Y., Shu R. Effects of alloying, heat treatment and nanoreinforcement on mechanical properties and damping performances of Cu–Al-based alloys: A review. *Nanotechnology Reviews*, 2021, vol. 10, pp. 1560–1591. DOI: 10.1515/ntrev-2021-0101.

10. Zykova A.P., Tarasov S.Y., Chumaevskiy A.V., Kolubaev E.A. A review of friction stir processing of structural metallic materials: process, properties, and methods. *Metals*, 2020, vol. 10 (6), pp. 772–812. DOI: 10.3390/met10060772.

11. Dinaharan I., Kalaiselvan K., Akinlabi E.T., Davim J.P. Microstructure and wear characterization of rice husk ash reinforced copper matrix composites prepared using friction stir processing. *Journal of Alloys and Compounds*, 2017, vol. 718, pp. 150–160. DOI: 10.1016/j.jallcom.2017.05.117.

12. Kalashnikov K.N., Chumaevskii A.V., Ivanov A.N. Producing high-strength materials by friction stir processing. *AIP Conference Proceedings*, 2018, vol. 2053, p. 040036. DOI: 10.1063/1.5084474.

13. Heidarzadeh A., Mironov S., Kaibyshev R., Çam G., Simar A., Gerlich A., Khodabakhshi F., Mostafaei A., Field D.P., Robson J.D., Deschamps A., Withers P.J. Friction stir welding/processing of metals and alloys: A comprehensive review on microstructural evolution. *Progress in Materials Science*, 2021, vol. 117, p. 100752. DOI: 10.1016/j.pmatsci.2020.100752.

14. Rahimzadeh A., Heidarzadeh A., Mohammadzadeh A., Moeini G. Effect of friction stir welding heat input on the microstructure and tensile properties of Cu-Zn alloy containing disordered β phase. *Journal of Materials Research and Technology*, 2020, vol. 9 (5), pp. 11154–11161. DOI: 10.1016/j.jmrt.2020.08.010.

15. Arulmoni V.J., Ranganath M.S., Mishra R.S. Friction stir processed copper: a review. *International Research Journal of Sustainable Science & Engineering*, 2015, vol. 3 (8), pp. 1–11.

16. Narender M., Manoj A., Jakirahamed A.D. Study on defects repairing using friction stir technologies. *Materials Today: Proceedings*, 2021, vol. 44 (1), pp. 2373–2379. DOI: 10.1016/j.matpr.2020.12.441.

17. Kasraie M., Hosseini M., Danesh-Manesh H., Abbasi M. Production of Al–Sn bearing material by friction stir processing technique: structural evaluation and mechanical property. *Materials Research Express*, 2019, vol. 6 (2), p. 026503. DOI: 10.1088/2053-1591/aaea2f.

18. Leszczyńska-Madej B., Madej M., Hrabia-Wiśnios J., Węglowska A. Effects of the processing parameters of friction stir processing on the microstructure, hardness and tribological properties of SnSbCu bearing alloy. *Materials*, 2020, vol. 13 (24), pp. 5826–5841. DOI: 10.3390/ma13245826.

19. Cheremnov A.M. *Zakonomernosti formirovaniya struktury i svoistv mednykh splavov tribologicheskogo naznacheniya v usloviyakh kvazivyazkogo techeniya pri friktsionnoi peremeshivayushchei obrabotke*. Diss. kand. tekhn. nauk [Regularities of structure and properties formation of tribological copper alloys under quasi-viscous flow during friction stir processing. PhD eng. csi. Diss]. Tomsk, 2026. 155 p.

20. Cartigueyen S., Mahadevan K. Role of friction stir processing on copper and copper based particle reinforced composites – a review. *Journal of Materials Science & Surface Engineering*, 2015, vol. 2 (2), pp. 133–145.

21. Iwaszko J. New trends in friction stir processing: rapid cooling – a review. *Transactions of the Indian Institute of Metal*s, 2022, vol. 75, pp. 1681–1693. DOI: 10.1007/s12666-022-02552-2.

22. Patel M.S., Immanuel R.J., Rahaman A., Khan M.F., Jouiad M. Critical review on advanced cooling strategies in friction stir processing for microstructural control. *Crystals*, 2024, vol. 14 (7), pp. 655–678. DOI: 10.3390/cryst14070655.

23. Sree Sabari S., Malarvizhi S., Balasubramanian V. Influences of tool traverse speed on tensile properties of air cooled and water cooled friction stir welded AA2519-T87 aluminium alloy joints. *Journal of Materials Processing Technology*, 2016, vol. 237, pp. 286–300. DOI: 10.1016/j.jmatprotec.2016.06.015.

24. Fratini L., Buffa G., Shivpuri R. Mechanical and metallurgical effects of in process cooling during friction stir welding of AA7075-T6 butt joints. *Acta Materialia*, 2010, vol. 58 (6), pp. 2056–2067. DOI: 10.1016/j.actamat.2009.11.048.

25. Sedeghati A., Bouzary H. A study on the effect of cooling on microstructure and mechanical properties of friction stir-welded AA5086 aluminum butt and lap joints. *Proceedings of the Institution of Mechanical Engineers, Part L: Journal of Materials: Design and Applications*, 2017, vol. 233 (6), pp. 1156–1165. DOI: 10.1177/1464420717726562.

26. Behtaripour E., Jafarian H.R., Seyedein S.H., Park N., Eivani A.R. High-temperature tensile properties of friction stir processed AA2024 aluminum alloy under varying in situ cooling conditions. *Journal of Materials Research and Technology*, 2025, vol. 35, pp. 140–151. DOI: 10.1016/j.jmrt.2025.01.008.

27. Xu N., Chen L., Gu B.-k., Ren Z.-k., Song Q.-n., Bao Ye-f. Heterogeneous structure-induced strength and ductility synergy of α-brass subjected to rapid cooling friction stir welding. *Transactions of Nonferrous Metals Society of China*, 2021, vol. 31 (12), pp. 3785–3799. DOI: 10.1016/S1003-6326(21)65764-3.

28. Xu N., Ueji R., Fujii H. Enhanced mechanical properties of 70/30 brass joint by rapid cooling friction stir welding. *Materials Science and Engineering: A*, 2014, vol. 610, pp. 132–138. DOI: 10.1016/j.msea.2014.05.037.

29. Akbarpour M.R., Mirabad H.M., Gazani F., Khezri I., Chadegani A.A., Moeini A., Kim H.S. An overview of friction stir processing of Cu–SiC composites: Microstructural, mechanical, tribological, and electrical properties. *Journal of Materials Research and Technology*, 2023, vol. 27, pp. 1317–1349. DOI: 10.1016/j.jmrt.2023.09.200.

30. Ashrafi H., Shamanian M., Sanayei M., Farhadi F., Szpunar J.A. The impact of welding heat input on microstructure, micro-texture, and mechanical properties of stir zone in friction stir welded DP600 steel. *Materials Today Communications*, 2023, vol. 37, p. 107127. DOI: 10.1016/j.mtcomm.2023.107127.

31. Koldin A.V., Platonov N.I. Teploobmen pri struinom okhlazhdenii vysokotemperaturnoi poverkhnosti [Heat transfer during jet cooling of high-temperature surface]. *Vestnik Chelyabinskogo gosudarstvennogo universiteta = Bulletin of Chelyabinsk State University*, 2013, no. 25, pp. 48–51.

32. Zuckerman N., Lior N. Jet impingement heat transfer: physics, correlations, and numerical modeling. *Advances in Heat Transfer*, 2006, vol. 39, pp. 565–631. DOI: 10.1016/S0065-2717(06)39006-5.

33. Ameri A.A.H., Elewa N.N., Ashraf M., Escobedo-Diaz J.P. General methodology to estimate the dislocation density from microhardness measurements. *Materials Characterization*, 2017, vol. 131, pp. 324–330. DOI: 10.1016/j.matchar.2017.06.031.

34. Tongne A., Desrayaud C., Jahazi M., Feulvarch E. On material flow in Friction Stir Welded Al alloys. *Journal of Materials Processing Technology*, 2017, vol. 239, pp. 284–296. DOI: 10.1016/j.jmatprotec.2016.08.030.

35. Liu F.C., Nelson T.W. In-situ material flow pattern around probe during friction stir welding of austenitic stainless steel. *Materials and Design*, 2016, vol. 110, pp. 354–364. DOI: 10.1016/j.matdes.2016.07.147.

36. Heidarzadeh A., Saeid T., Klemm V., Chabok A., Pei Yu. Effect of stacking fault energy on the restoration mechanisms and mechanical properties of friction stir welded copper alloys. *Materials and Design*, 2019, vol. 162, pp. 185–197. DOI: 10.1016/j.matdes.2018.11.050.

37. Lee S., Baek S., Lee S.-J., Chen C., Nishijima M., Suganuma K., Utsunomiya H., Ma N., Yu H.-Y., Kim D. Driving forces of solid-state Cu-to-Cu direct bonding suppressing the work-hardening loss by refill friction stir spot welding. *Materials Science and Engineering: A*, 2024, vol. 915, p. 147178. DOI: 10.1016/j.msea.2024.147178.

Conflicts of Interest

The authors declare no conflict of interest.